(Received 30 May 2026, Accepted 17 June 2026, Scheduled 3 July 2026)

A Compact Multi-Band MIMO Antenna for Sub-6 GHz and 5G Millimeter-Wave Communications

Chenglong Xiao[1], Ming Yang[1,*], Jinzhi Zhou[2], and Qing Liu[1]

[1] *School of Electronic Information and Artificial Intelligence, West Anhui University, Lu'an 237012, China*
[2] *Department of Electronic and Information Engineering, Bozhou University, 236800, China*

ABSTRACT: A miniaturized multi-band MIMO antenna for Sub-6 GHz and 5G mmWave is proposed. The antenna is composed of a C-shaped radiating element and coupled ground branches. Tri-band coverage is achieved (4.37–5.88 GHz, 23.5–32.89 GHz, and 36.8–40.1 GHz) through the optimization of the dimensions of the C-shaped antenna and the incorporation of a cross-shaped structure. The low-frequency band fully covers the n79 (4.4–5 GHz) band, as well as the Wi-Fi 5/6 (5.15–5.85 GHz) and 5 GHz ISM (5.725–5.875 GHz) bands. The mid-frequency band completely covers the 5G mmWave n257 (26.5–29.5 GHz), n258 (24.25–27.5 GHz), and n261 (27.5–28.35 GHz) bands, while the high-frequency band fully covers the n260 (37–40 GHz) band. Measured results show gains of approximately 0.95 dBi, 5.89 dBi, and 8.83 dBi in the low-, mid-, and high-frequency bands, respectively. Inter-element isolation is found to be better than −20 dB, and the ECC is < 0.003. The antenna is characterized by a compact size, simple structure, and multi-band coverage, making it suitable for cooperative communication between Sub-6 GHz and 5G mmWave bands.

1. INTRODUCTION

With the large-scale commercialization of the fifth-generation (5G) mobile communication system, mobile data traffic has grown exponentially, placing greater demands on system capacity and transmission rates. To meet the requirements of diverse application scenarios, including enhanced Mobile Broadband (eMBB), Ultra-Reliable Low-Latency Communication (URLLC), and Massive Machine-Type Communication (mMTC), a spectrum-layered deployment strategy has been adopted, covering the Sub-6 GHz and millimeter-wave (mmWave) bands [1, 2]. According to the 5G frequency band standards defined by 3GPP, the n79 band (4.4–5 GHz) in the FR1 band is the mainstream spectrum resource for global 5G deployment, and it is widely applied in urban macro base stations, hotspot coverage, and enterprise private networks. In the FR2 band, the n257 (26.5–29.5 GHz), n258 (24.25–27.5 GHz), n260 (37–40 GHz), and n261 (27.5–28.35 GHz) bands are the core spectrum resources for achieving high-data-rate applications, such as Fixed Wireless Access (FWA) and Virtual Reality (VR)/Augmented Reality (AR) [3].

Millimeter-wave (mmWave) communication technology, owing to its abundant continuous bandwidth resources, has become one of the key enabling technologies for 5G and future 6G mobile networks [4]. However, the high path loss, atmospheric absorption, and susceptibility to blockage in the mmWave band pose severe challenges to antenna systems [5]. Multiple-Input Multiple-Output (MIMO) technology, in which multiple radiating elements are integrated within a limited space and spatial, polarization, and pattern diversity are exploited and can significantly enhance channel capacity and link reliability, serving as an effective solution to these challenges [6]. In recent years, tremendous efforts have been devoted to the development of 5G MIMO antennas, yielding substantial research achievements.

How to effectively improve the isolation of MIMO antennas has long been a key research focus in this field. In [7], a high-isolation four-port MIMO antenna was realized through orthogonal polarization and a Defected Ground Structure (DGS), which covers the n79 band with port isolation better than −18 dB. To meet the specialized design requirements of the n79 band, Ref. [8] employed a novel unequal-length stub-DGS on a compact substrate to achieve stable full-band coverage of the n79 band, while improving the port isolation to above −20 dB and reducing the envelope correlation coefficient (ECC) to below 0.01. In [9], DGS combined with ground branches was employed to achieve high isolation of −29 dB and −41.4 dB at 3.5 GHz and 4.85 GHz, respectively. In [10], parasitic patches were introduced between MIMO elements, enhancing isolation above −25 dB across the ultra-wideband range of 2.3–17.8 GHz and providing a new implementation path for decoupling design in MIMO antennas.

To further enhance system capacity, Ref. [11] realized a co-aperture antenna with an 8-port Sub-6 GHz MIMO and a 4-port 5G mmWave MIMO on an octagonal substrate, with the dual bands covering n79/n257/n258 bands, thereby verifying the feasibility of high-density integration. For Ultra-Wideband (UWB) applications, four-port UWB MIMO antennas with octagonal and annular structures were designed in [12, 13], with operating bandwidths covering 2.5–16.7 GHz and 2.5–10.6 GHz, respectively, and achieving port isolation better than −18 dB and envelope correlation coefficient (ECC) lower than 0.03, providing technical references for multi-band fusion de-

* Corresponding author: Ming Yang (myang@ahu.edu.cn).

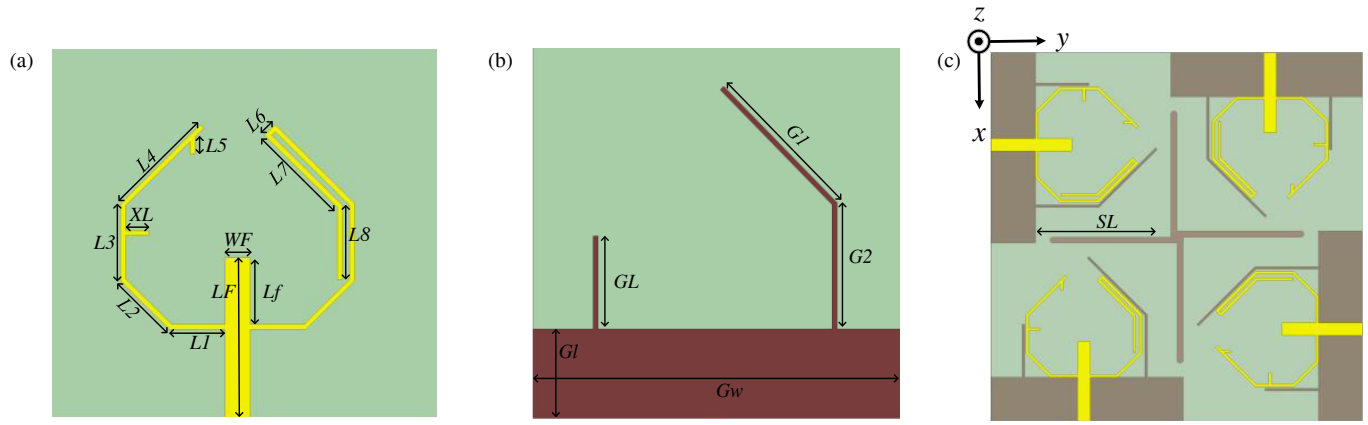

FIGURE 1. Schematic of the antenna structure. (a) Top view, (b) bottom view, and (c) overall view.

sign. In accordance with the work in [14], ultra-wideband performance covering 2.92–16.97 GHz was realized on a miniaturized substrate through a fractal slot structure and composite decoupling technique, while excellent isolation and low correlation were maintained across the entire operating band, further enriching the design schemes of 5G multi-band fusion antennas.

Besides microstrip antennas, various design approaches have been employed to realize broadband mmWave antennas. An antenna-in-package (AiP) structure for Ka-band 5G communications is proposed in [15], achieving a return loss bandwidth of 0.8 GHz and a peak gain of 3.8 dBi at 30.5 GHz, while supporting both horizontal and vertical dual polarizations. A millimeter-wave longitudinal slot array antenna based on double-sided integrated suspended line (DSISL) is presented in [16], achieving an impedance bandwidth of 19.3% over the 25.8–31.3 GHz band, with a maximum measured gain of 20.2 dBi and a radiation efficiency of 93%. A four-port MIMO antenna integrated with a metasurface and a frequency-selective surface is reported in [17], achieving a wide bandwidth of 24–50 GHz and isolation exceeding −33 dB, thereby demonstrating the feasibility of combining miniaturization and broadband performance. A 0.76 mm ultra-thin 2×2 dipole array antenna for 5G mmWave applications is designed in [18], employing a tightly coupled frequency-selective surface, a capacitively coupled feeding method, and H-shaped walls to cover the 24–40 GHz frequency range. Ref. [19] presents a bowtie antenna fed by a coplanar waveguide, achieving a relative bandwidth of 33.35% (34.62–47.96 GHz) at the center frequency of 40 GHz. In [20], the impedance bandwidth of a 1×4 array is extended to 28% (23–30.5 GHz) by loading a 2×3 parasitic square patch array, fully covering the n257, n258, and n261 bands and enabling a beam-scanning capability of $\pm 40°$. Wideband coverage of the Sub-6 GHz and mmWave bands is achieved in [21] through a composite radiating structure, verifying the feasibility of full-band integrated design; however, the relatively large size of the design limits its suitability for system integration.

Although significant progress has been achieved in the above studies, realizing coverage of the Sub-6 GHz and 5G mmWave bands within a limited space, while maintaining high isolation and broadband performance, remains a core challenge in current MIMO antenna design. To this end, a miniaturized multi-band Sub-6 GHz and 5G mmWave MIMO antenna is designed. The antenna has dimensions of $30 \times 30 \times 0.787\ \text{mm}^3$ ($2.5\lambda_0 \times 2.5\lambda_0 \times 0.066\lambda_0$), where λ_0 is the free space wavelength at the operating frequency of 25 GHz, and tri-band coverage (4.37–5.88 GHz, 23.5–32.9 GHz, and 36.8–40.1 GHz) is achieved through the optimization of the radiating and ground structures.

2. SINGLE-ANTENNA DESIGN

2.1. Antenna Structure

The single-antenna structure of the proposed broadband multi-band MIMO antenna is shown in Fig. 1. The antenna dimensions are initially estimated based on $\lambda/2$ or $\lambda/4$ corresponding to the target resonant frequencies. The dimensions of each structural component are then optimized using High Frequency Structure Simulator (HFSS), and the final optimized dimensions are presented in Table 1. Fig. 1(a) shows the front view of the antenna, where the single antenna exhibits a C-shaped structure composed of three branches. By optimizing the three branches of the radiating patch, multiple resonant points in the mid- and high-frequency ranges of the 5G mmWave band can be excited. Fig. 1(b) presents the back view of the antenna, where the addition of two coupled ground branches effectively extends the low-frequency bandwidth of the antenna. Fig. 1(c) illustrates the overall structure of the four-port antenna, in which a cross-shaped structure is added at the center of the antenna to significantly enhance the isolation between antenna elements.

TABLE 1. Dimensional parameters of the antenna.

Parameter	*L1*	*L2*	*L3*	*L4*	*L5*	*XL*
Value (mm)	2.23	2.755	3.15	4.5	0.7	0.94
Parameter	*L6*	*L7*	*L8*	*LF*	*WF*	*Lf*
Value (mm)	0.6	4	3	6.5	1	2.7
Parameter	*GL*	*GL1*	*GL2*	*GL*	*Gw*	*SL*
Value (mm)	4.3	5.1	6.65	3.6	15.5	10

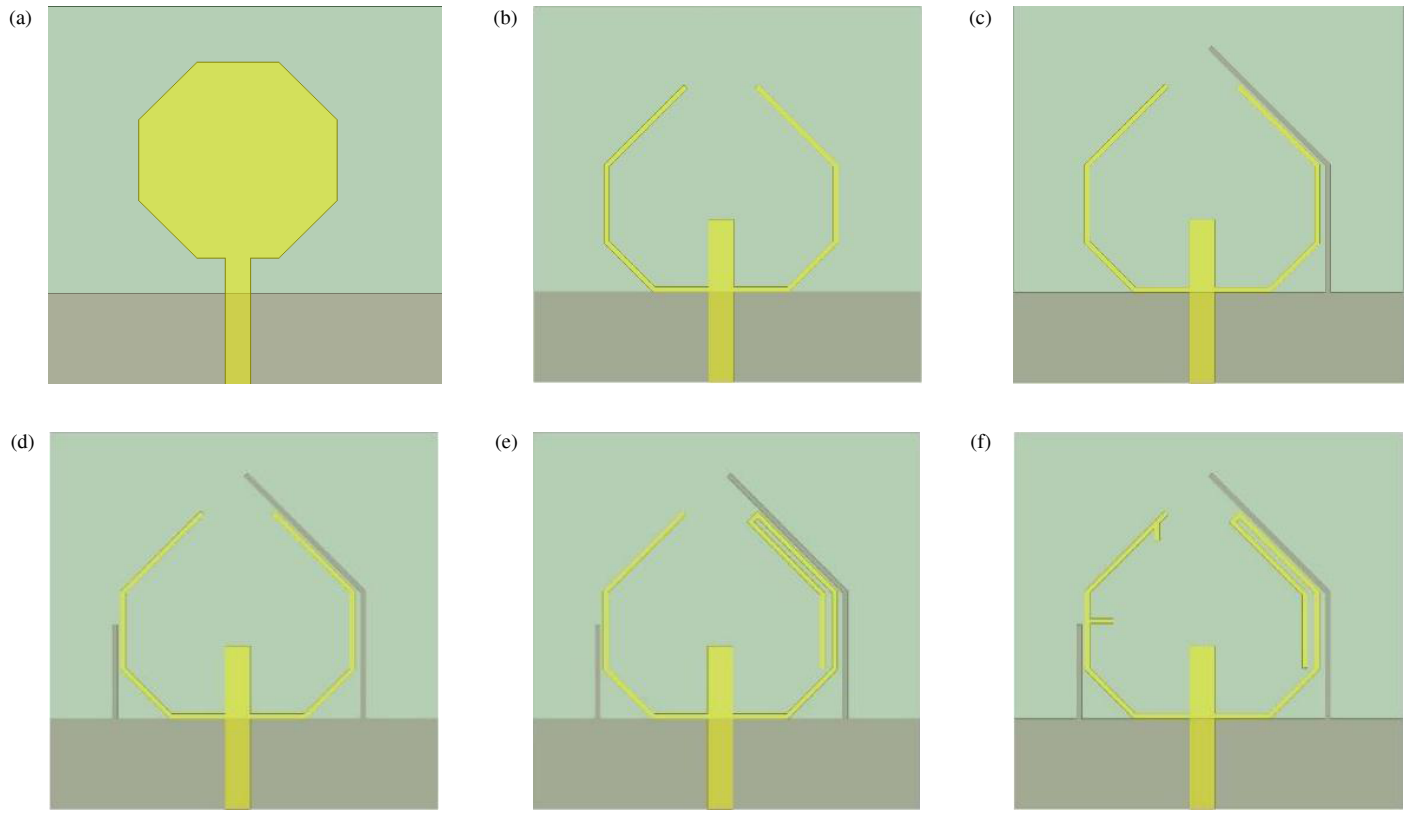

FIGURE 2. Structural evolution of the single antenna. (a) Ant 1, (b) Ant 2, (c) Ant 3, (d) Ant 4, (e) Ant 5, and (f) Ant 6.

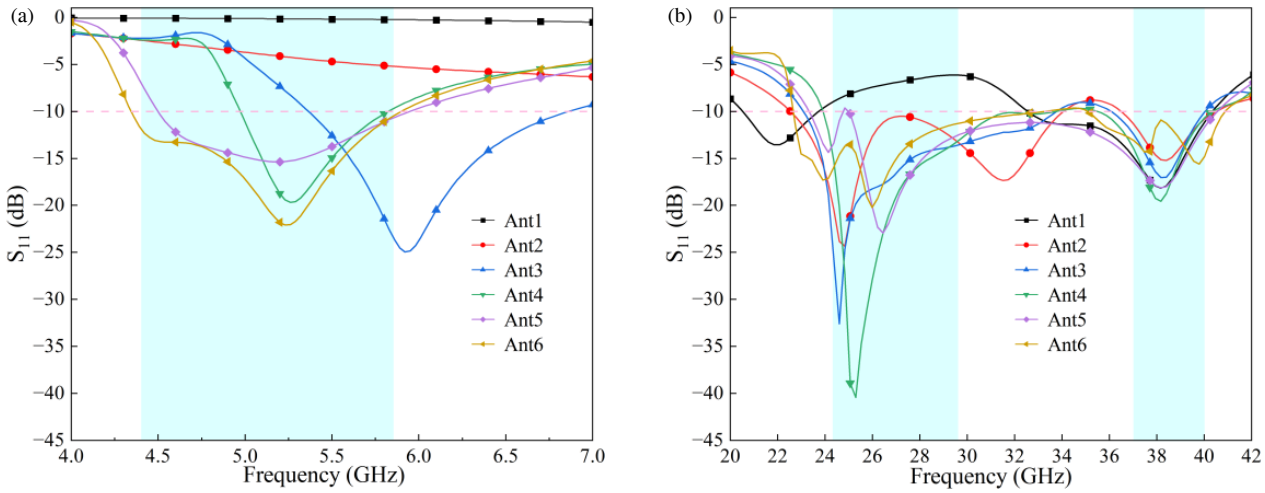

FIGURE 3. Simulated S-parameters of Ant 1-Ant6. (a) Sub-6 GHz S_{11} and (b) 5G mmWave S_{11}.

2.2. Evolution of the Antenna Design

The single-antenna structure is iteratively optimized through six design stages. The antenna structures at each stage are shown in Fig. 2, and the corresponding reflection coefficient S_{11} performance is presented in Fig. 3.

As shown in Fig. 2(a), an octagonal monopole antenna, denoted as Ant 1, is constructed on a metallic ground plane. This antenna generates a resonant point at 39 GHz. Under the condition of $S_{11} < -10$ dB, Ant 1 is able to cover the 32.56–41.54 GHz frequency range, meeting the coverage requirement of the 5G mmWave n260 high-frequency band; however, it still cannot satisfy the coverage requirements of the low- and mid-frequency bands. As shown in Fig. 2(b), two additional branches are added to Ant 1 to form a C-shaped antenna, denoted as Ant 2. The impedance bandwidth in the mid-frequency band is significantly extended. As shown in Fig. 3(b), under the condition of $S_{11} < -10$ dB, Ant 2 is able to cover the 23–34.05 GHz frequency range, meeting the mid-frequency communication requirements of the 5G mmWave n257/n258/n261 bands.

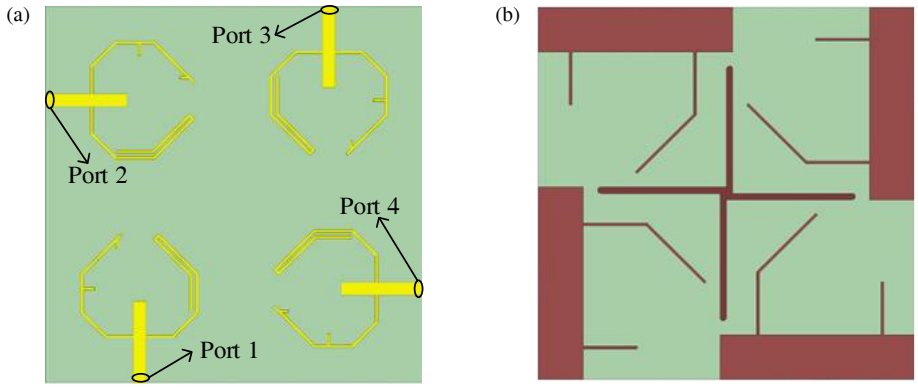

FIGURE 4. Four-port MIMO antenna structure. (a) top view and (b) bottom view.

To achieve low-frequency coverage in the Sub-6 GHz band, two ground branches are introduced based on Ant 2, as shown in Figs. 2(c) and 2(d), denoted as Ant 3 and Ant 4, respectively. The introduction of the ground branches alters the antenna's current path. As shown in Fig. 3(a), after the gradual introduction of the two ground branches, a new resonant point is generated at 6 GHz and shifts toward lower frequencies. Under the condition of $S_{11} < -10$ dB, the antenna is able to cover the 4.96–5.83 GHz frequency range, satisfying the coverage requirements of the Wi-Fi 5/6 and 5 GHz ISM bands; however, the bandwidth remains narrow and cannot meet the low-frequency communication requirement of the Sub-6 GHz n79 band.

To further broaden the low-frequency communication range, as shown in Fig. 2(e), the right branch of the C-shaped structure in Ant 4 is extended downward using a bending technique, resulting in Ant 5. This modification alters the antenna's current path and generates a new resonant point at 4.75 GHz, further extending the low-frequency bandwidth. As shown in Fig. 3(a), under the condition of $S_{11} < -10$ dB, the antenna is able to cover the 4.5–5.95 GHz range. As shown in Fig. 2(f), two short branches are added to the left branch of the C-shaped patch, producing the final designed antenna, denoted as Ant 6. A resonant point is generated at 4.4 GHz in the low-frequency band by loading the short branches, thereby extending the low-frequency bandwidth and improving the impedance matching in the mid-frequency band. As shown in Fig. 3(a), from the S_{11} curve, it can be observed that the resonant characteristics in the low-frequency band are further optimized, with the low-frequency resonant point shifting toward lower frequencies. Under the condition of $S_{11} < -10$ dB, the antenna is able to cover the 4.36–5.91 GHz range in the low-frequency band.

Based on the optimization results from the six design stages, Ant 6 finally achieves tri-band coverage of 4.36–5.91 GHz, 23.81–33.72 GHz, and 36.84–40.47 GHz, with the reflection coefficient in each band satisfying the condition of $S_{11} < -10$ dB.

2.3. Design and Analysis of the MIMO Antenna

The final proposed multi-band MIMO antenna is shown in Fig. 4, with Fig. 4(a) presenting the front view and Fig. 4(b) the back view. The antenna is fabricated on a Rogers RT-5880 substrate with low transmission loss and stable dielectric properties, having a thickness of 0.787 mm, a relative permittivity of $\varepsilon_r = 2.2$, and a loss tangent of $\tan\delta = 0.009$. The overall dimensions of the antenna are $30 \times 30 \times 0.787\,\text{mm}^3$. Four C-shaped antenna elements are symmetrically placed at the center of the substrate surface, and an orthogonal layout is employed to preliminarily suppress mutual coupling between the antenna elements. A cross-shaped structure is designed at the center of the substrate, further reducing the mutual coupling effects between the antennas.

To verify the improvement in MIMO antenna isolation provided by the cross-shaped structure on the substrate, simulations were conducted for two cases: with and without the cross-shaped structure. Figs. 5(a) and 5(b) show the S-parameters of the antenna without a cross-shaped structure, where Fig. 5(a) presents the Sub-6 GHz S-parameter curves, and Fig. 5(b) presents the mmWave S-parameter curves. Figs. 6(a) and 6(b) show the S-parameters in the corresponding frequency bands after the cross-shaped structure is added.

As shown in Figs. 5(a) and 6(a), the presence or absence of the cross-shaped structure does not affect the antenna isolation in the low-frequency band of 4.36–5.91 GHz, with the S-parameters remaining below -20 dB. As observed from Fig. 5(b), in the mmWave mid-frequency band of 23.81–33.72 GHz, the antenna without the cross-shaped structure exhibits an isolation of approximately -16 dB at 25 GHz. After the cross-shaped structure is added, the antenna isolation is significantly improved. As shown in Fig. 6(b), the isolation in the mid-frequency band of 23.81–33.72 GHz reaches approximately -30 dB.

2.4. Parametric Analysis

According to the surface current distribution analysis, the branch lengths associated with SL, XL, and GL are found to have significant effects on the antenna bandwidth and isolation performance. Therefore, in order to further analyze the performance of the antenna, this paper separately analyzes the key parameters of the arm length SL of the cross-shape structure, the short branch length XL of the C-shape radiating element, and the length of the left grounding branch GL.

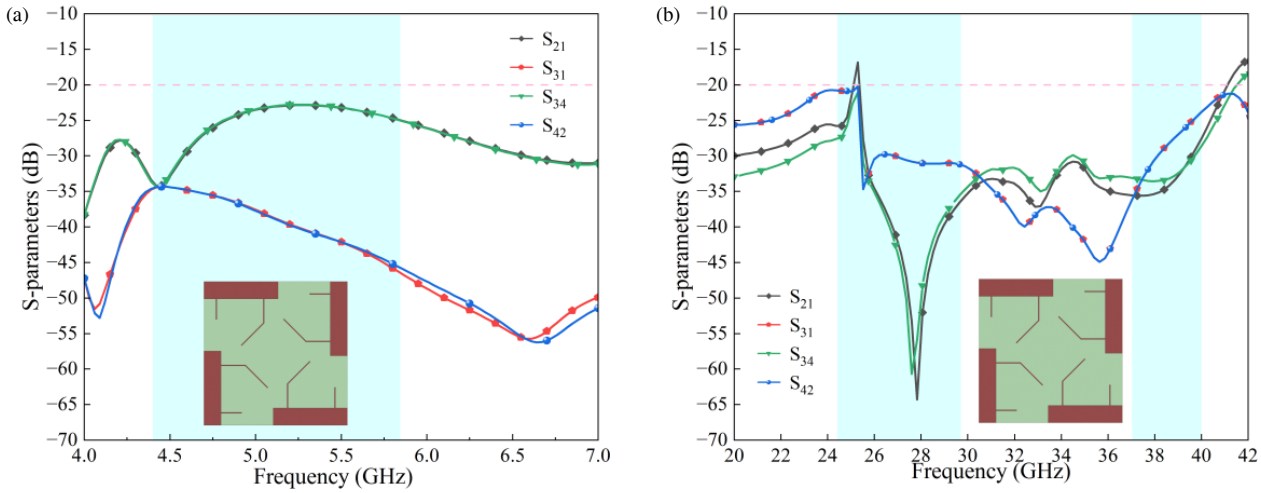

FIGURE 5. Isolation of the MIMO antenna without the cross-shaped structure. (a) Sub-6 GHz S-parameters and (b) 5G mmWave S-parameters.

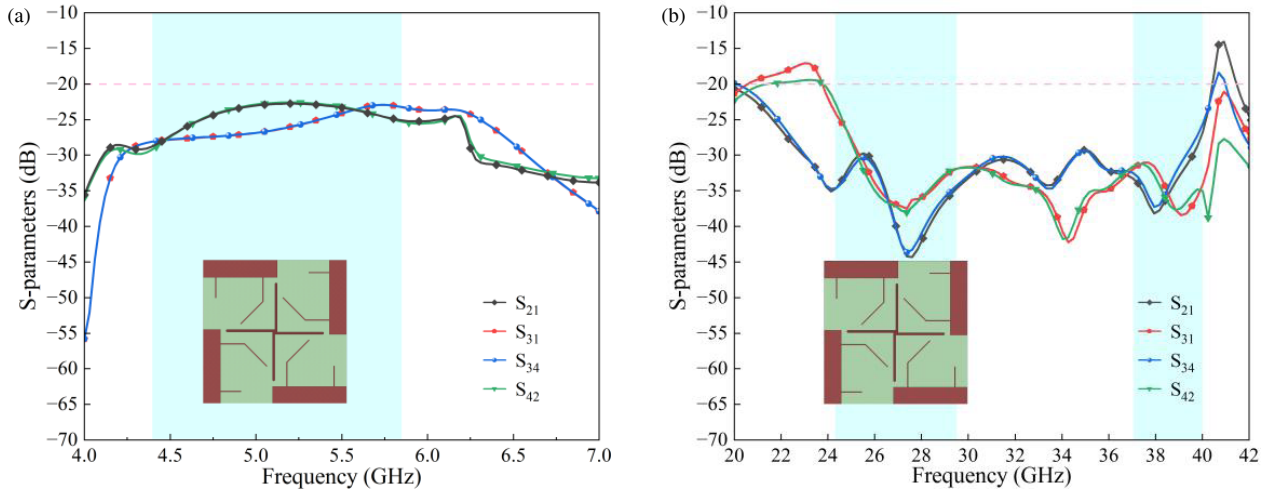

FIGURE 6. Isolation of the MIMO antenna with the cross-shaped structure. (a) Sub-6 GHz S-parameters and (b) 5G mmWave S-parameters.

The cross-shaped structure is located at the center of the four-element MIMO antenna, and its arm length SL is the key parameter determining port isolation performance. Three values of $SL = 8$ mm, 10 mm, and 12 mm are selected for parametric sweep analysis. Due to the antenna's symmetry, only the isolation between adjacent ports and diagonal ports is analyzed. The results of the parametric scan are shown in Fig. 7, where Figs. 7(a) and 7(b) present the changes in the adjacent-port isolation S_{21} for the Sub-6 GHz and 5G mmWave bands, respectively, and Figs. 7(c) and 7(d) show the changes in the diagonal-port isolation S_{42} for the Sub-6 GHz and 5G mmWave bands. The design requirement for all port isolations is better than -20 dB.

When $SL = 8.0$ mm, the adjacent-port isolation S_{21} in the low-, mid-, and high-frequency bands is better than -20 dB, while the diagonal-port isolation S_{42} at 25 GHz in the mid-frequency band is only -13 dB. This has a significant impact on diagonal-port isolation in the mid-frequency band and clearly does not meet the requirement. When $SL = 10$ mm, S_{42} in the low- and high-frequency bands satisfies the isolation requirement of better than -20 dB, and the isolation at 25 GHz in the mid-frequency band is improved. When SL is further increased to 12 mm, the isolations of S_{21} and S_{42} at 4.5 GHz in the low-frequency band deteriorate significantly, failing to meet the requirement of isolation below -20 dB. Therefore, only when $SL = 10$ mm are S_{21} and S_{42} stably better than -20 dB in the low-, mid-, and high-frequency bands, ultimately achieving the optimal isolation performance.

The length of the short branch XL of the C-shaped radiating element primarily regulates the operating bandwidth in the low-frequency band, while also affecting the bandwidth in the high-frequency band. Three sets of parameters with $XL = 0.64$ mm, 0.94 mm, and 1.24 mm are selected for parametric sweep analysis. The results are shown in Fig. 8, where Fig. 8(a) presents the S_{11} curves for the Sub-6 GHz band, and Fig. 8(b) presents the S_{11} curves for the 5G mmWave band.

When $XL = 0.64$ mm, the left portion of the low-frequency band is narrow, preventing complete coverage of the n79 band. As XL is increased to 0.94 mm, the resonant points shift toward lower frequencies, and the bandwidth is extended, achieving coverage from 4.4 to 5.85 GHz, which meets the requirements of the n79, Wi-Fi 5/6, and 5 GHz ISM bands. When XL is fur-

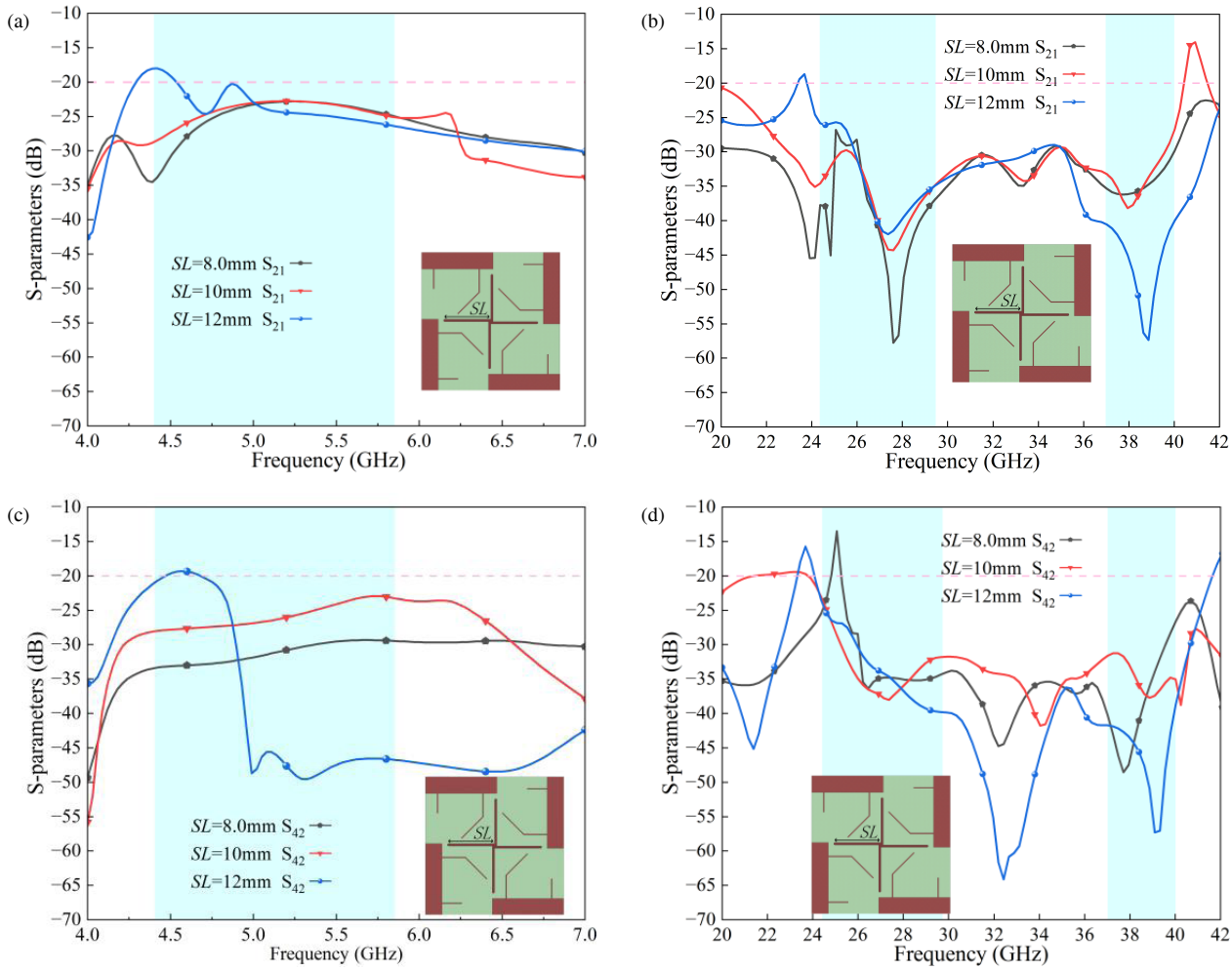

FIGURE 7. Effect of the arm length SL of the cross-shaped structure on antenna isolation. (a) Sub-6 GHz S_{21}, (b) 5G mmWave S_{21}, (c) Sub-6 GHz S_{42}, and (d) 5G mmWave S_{42}.

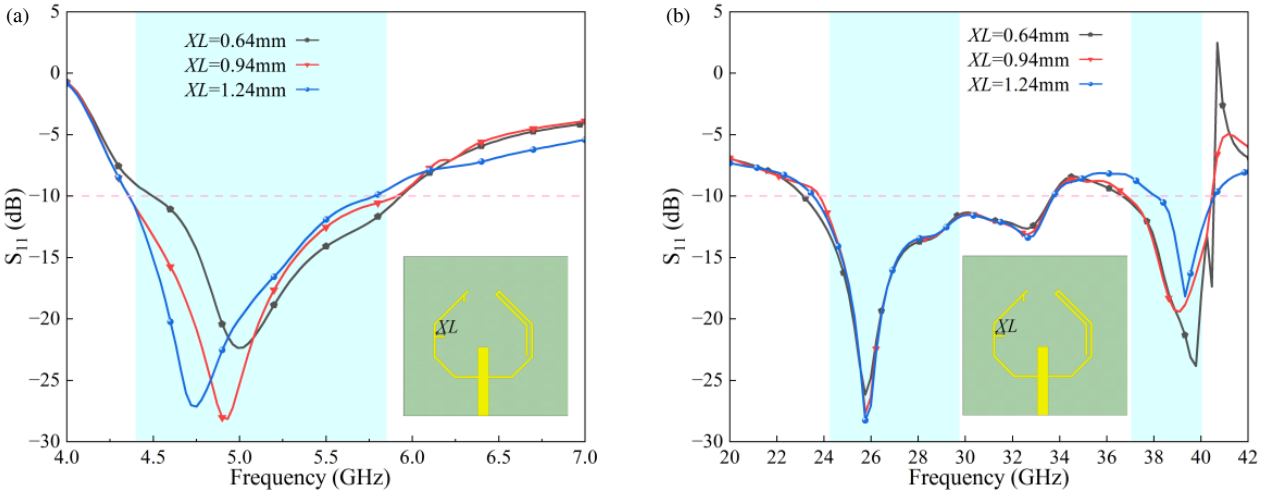

FIGURE 8. Effect of the short branch length XL of the C-shaped radiating element on S_{11}. (a) Sub-6 GHz and (b) 5G mmWave.

ther increased to 1.24 mm, the resonant frequencies continue to shift to lower frequencies, and the right portion of the low-frequency band becomes narrow, preventing full coverage of the Wi-Fi 5/6 and 5 GHz ISM bands. Meanwhile, the high-frequency band bandwidth also becomes narrower and cannot fully cover the n260 band. Therefore, $XL = 0.94$ mm is selected as the optimal value.

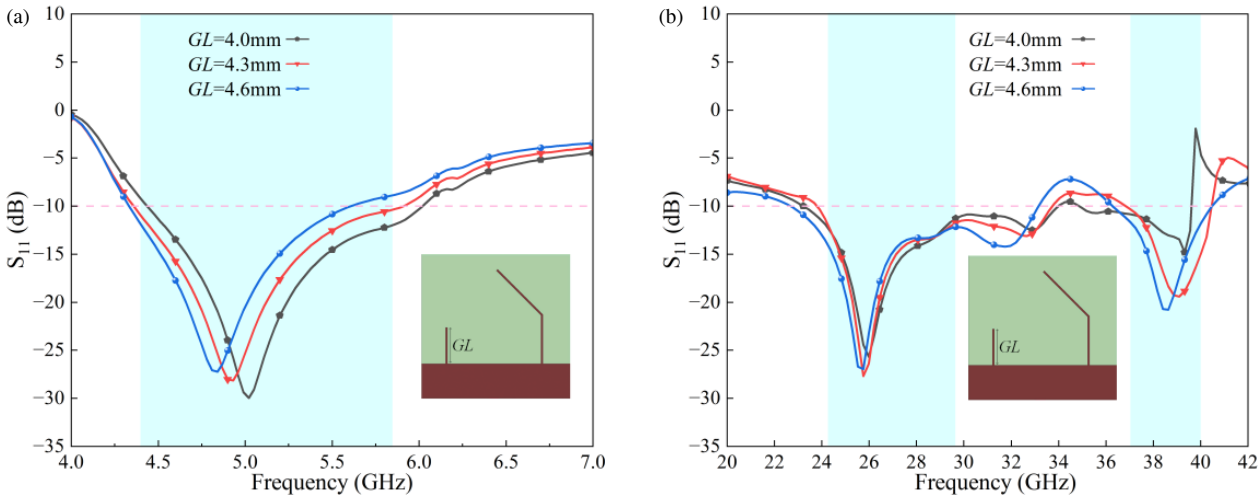

FIGURE 9. Effect of the left ground branch length GL on S_{11}. (a) Sub-6 GHz and (b) 5G mmWave.

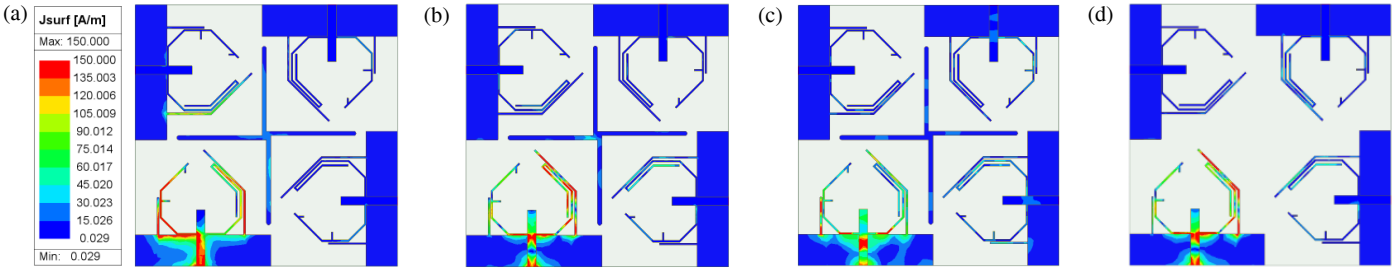

FIGURE 10. Surface current distribution. (a) $f = 4.902$ GHz, (b) $f = 25.807$ GHz, (c) $f = 39.032$ GHz, and (d) $f = 25.807$ GHz.

The left ground branch GL is located on the left ground plane of the antenna and forms capacitive coupling with the left branch of the C-shaped radiating element, significantly affecting the antenna performance. The length of GL can regulate the resonant points and bandwidth in the low-frequency band, while also influencing the bandwidth in the high-frequency band. Three values of $GL = 4.0$ mm, 4.3 mm, and 4.6 mm are selected for parametric sweep analysis, as shown in Fig. 9, where Fig. 9(a) presents the S_{11} curves for the Sub-6 GHz band, and Fig. 9(b) presents the S_{11} curves for the 5G mmWave band.

In the low-frequency band, when $GL = 4.0$ mm, the bandwidth cannot fully cover the n79 band. When GL is increased to 4.3 mm, the antenna resonant points shift toward lower frequencies, and the operating bandwidth covers 4.36–5.91 GHz, satisfying the requirements of the n79, Wi-Fi 5/6, and 5 GHz ISM bands. When GL is further increased to 4.6 mm, the low-frequency resonant points continue to shift leftward, and the operating bandwidth becomes significantly narrower, failing to meet the design requirements. In the mid- and high-frequency bands of the 5G mmWave spectrum, only when $GL = 4.0$ mm does the antenna fail to fully cover the n260 band. These results indicate that an appropriately sized ground branch can form effective capacitive coupling with the left branch of the unit antenna, achieving an extension of the low-frequency bandwidth. However, an excessively long ground branch introduces additional parasitic coupling, deteriorating matching and affecting the bandwidth in both the low- and high-frequency bands. Therefore, $GL = 4.3$ mm is selected as the optimal value.

Based on the performance analysis of the three key parameters, the final key parameters of the antenna are determined as follows: the arm length of the cross-shaped structure $SL = 10$ mm, the short branch length of the C-shaped radiating element $XL = 0.94$ mm, and the length of the left ground branch $GL = 4.3$ mm. The antenna ultimately achieves tri-band coverage in the low-frequency band (4.36–5.91 GHz), mid-frequency band (23.81–33.72 GHz), and high-frequency band (36.84–40.47 GHz), with port isolation better than -20 dB.

2.5. Surface Current Distribution

To illustrate the multi-band radiation mechanism and port isolation of the designed antenna, the surface current distributions of a single antenna are simulated at three resonant frequencies, 4.902 GHz, 25.807 GHz, and 39.032 GHz, under the condition that only Port 1 is excited, and the remaining ports are terminated with 50 Ω matched loads. The results are shown in Fig. 10.

Figure 10(a) shows the surface current distribution of the single antenna at the resonant frequency of 4.902 GHz. As observed from the figure, the strong currents are almost entirely concentrated on the C-shaped antenna and the coupled ground branches on both sides. No significant strong currents are ob-

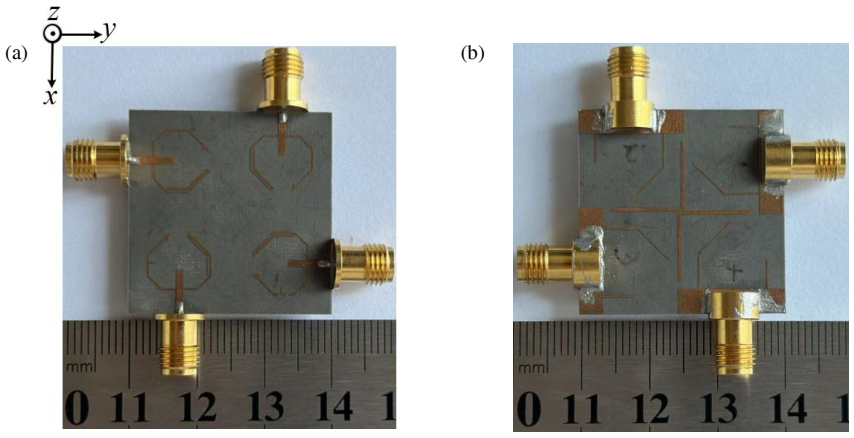

FIGURE 11. Prototype of the fabricated MIMO antenna. (a) Top view and (b) bottom view.

served on the other three non-excited radiating elements or on the cross-shaped structure. The simulation results indicate that the radiation at this frequency is entirely dominated by the C-shaped antenna and the coupled ground branches, and they also confirm that the cross-shaped structure provides excellent decoupling in the low-frequency band, effectively suppressing mutual coupling between the antennas.

Figure 10(b) shows the surface current distribution of the single antenna at the resonant frequency of 25.807 GHz. As observed from the figure, the strong currents are concentrated at the base of the unit antenna, the right folded branch, and the right coupled ground branch, while the feeding connection still maintains relatively high current density. These results indicate that the resonance at this frequency is dominated by certain branches of the single antenna. The shift in the strong current distribution reflects the independent tuning characteristic of the antenna's multi-frequency resonances, which essentially corresponds to the switching of the dominant radiation characteristic modes at different frequencies [22]. Meanwhile, the weak induced currents on the cross-shaped structure form cancellation paths that oppose the coupling currents between the unit antennas, achieving high isolation in this frequency band. This decoupling mechanism is fully consistent with the core design principle of mutual coupling cancellation in MIMO antennas for mobile communications [23]. The surface current distribution at 25.807 GHz without the cross-shaped structure is shown in Fig. 10(d). It can be observed that significant induced currents are present on the ground branches of the diagonal antenna element, indicating strong mutual coupling between the antenna elements. This result further confirms that the cross-shaped structure is effective for significantly enhancing the isolation performance of the antenna.

The surface current distribution of the single antenna at the resonant frequency of 39.032 GHz is shown in Fig. 10(c). As observed from the figure, the currents are not evenly distributed across the branches; instead, they are highly concentrated at the root region of the excited single antenna and the left-coupled ground branch. These results indicate that, at this frequency, the left-coupled ground branch and bottom-feeding region together constitute the primary radiation path of the antenna in the high-frequency band, which corresponds to the higher-order characteristic radiation mode of the antenna at this frequency.

3. RESULTS AND DISCUSSION

3.1. Simulation and Measurement

The antenna prototype is fabricated based on the optimized model dimensions, as shown in Fig. 11. Fig. 11(a) is the top view, and Fig. 11(b) is the bottom view. Due to the high propagation loss of millimeter-wave signals, substrates with low dielectric constants are generally preferred. Therefore, the proposed antenna is fabricated on a Rogers RT-5880 substrate with a thickness of 0.787 mm, a relative permittivity of $\varepsilon_r = 2.2$, and a loss tangent of $\tan\delta = 0.0009$. The substrate features low transmission loss and stable dielectric properties. The simulated and measured reflection coefficients S-parameters of the antenna are shown in Fig. 12, where Fig. 12(a) presents the Sub-6 GHz S-parameter results, and Fig. 12(b) presents the 5G mmWave S-parameter results.

As shown in Fig. 12, the measured bandwidth of the antenna in terms of S_{11} is narrower than its simulated counterpart. This discrepancy is mainly attributed to soldering tolerances and practical measurement errors. Nevertheless, the measured results are basically in good agreement with the simulated ones. For $S_{11} < -10$ dB, three operating frequency bands are achieved, covering 4.37–5.88 GHz, 23.5–32.89 GHz, and 36.8–40.1 GHz, with both the simulated and measured port isolations maintained below -20 dB. This further verifies the favorable impedance-matching performance of the proposed antenna.

3.2. Radiation Characteristics

The radiation performance of the antenna is tested in a microwave anechoic chamber, as shown in Fig. 13. In this section, three resonant frequencies of the antenna in low-, mid-, and high-frequency bands, i.e., 4.902 GHz, 25.807 GHz, and 39.032 GHz, are selected for measurement, and the radiation performance of the antenna is analyzed accordingly. Fig. 14 presents the two-dimensional radiation patterns in the xoz, yoz, and xoy planes for each resonant frequency. Figs. 14(a)–(c)

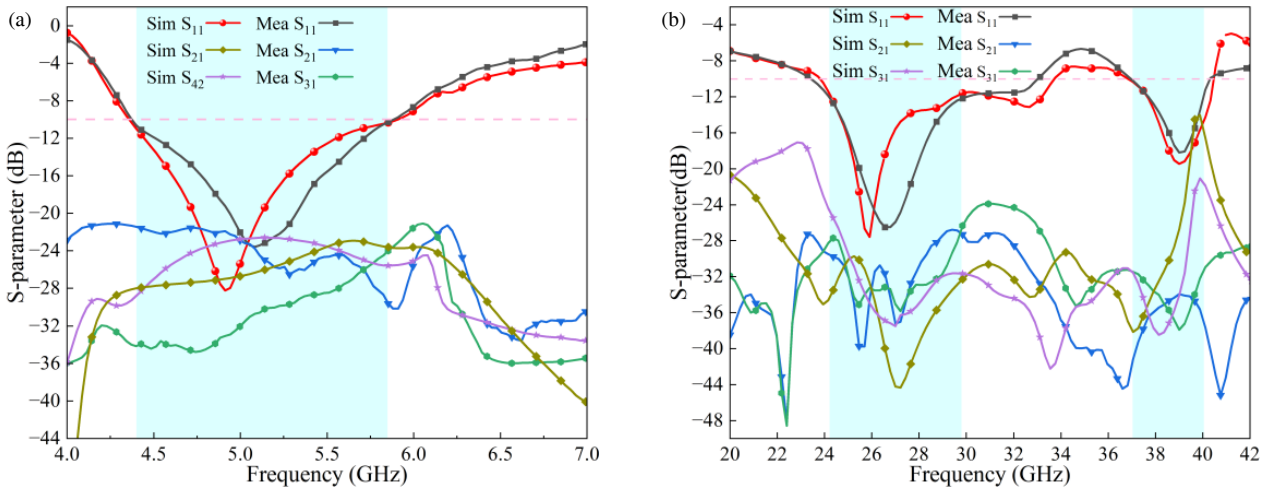

FIGURE 12. Simulated and measured S-parameters of the MIMO antenna. (a) Sub-6 GHz and (b) 5G mmWave.

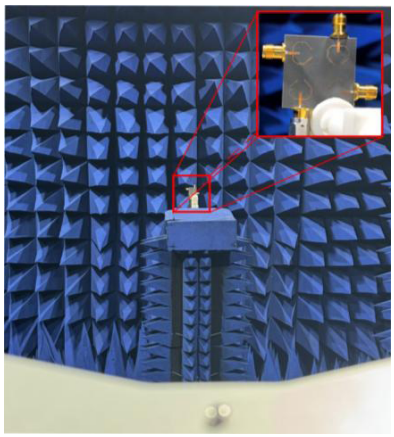

FIGURE 13. Anechoic chamber diagram.

correspond to the three planes at the 4.902 GHz resonant frequency, while Figs. 14(d)–(f) and 14(g)–(i) correspond to the three planes at the 25.807 GHz and 39.032 GHz resonant frequencies, respectively.

As observed from the figures, in the low-frequency band of 4.902 GHz, the antenna exhibits omnidirectional radiation characteristics in all planes, with smooth and clean waveforms and no significant sidelobe interference, demonstrating excellent spatial coverage. In the mid-frequency band at 25.807 GHz, the antenna maintains a high degree of consistency with the low-frequency band, with a clearly defined and controllable main radiation direction. At the high frequency of 39.032 GHz, the antenna still maintains certain radiation performance, with the yoz and xoz planes exhibiting multi-directional radiation patterns.

Overall, the antenna exhibits good consistency in radiation performance across the operating frequency bands, confirming its excellent cross-polarization suppression capability. The overall radiation performance is sufficient to meet the requirements of high-speed transmission applications in the Sub-6 GHz and 5G mmWave bands.

3.3. Envelope Correlation Coefficient

Envelope correlation coefficient (ECC) is a key metric for evaluating the signal independence between ports of a MIMO antenna. A lower ECC indicates weaker correlation between the signals received by the antenna elements and better diversity performance [24]. For a four-port MIMO antenna, ECC can be calculated from far-field radiation patterns, as expressed in Equation (1):

$$rho_{ij} = \frac{\left|\iint_{4\pi} F_i(\theta,\phi)\cdot F_j^*(\theta,\phi)\,d\Omega\right|^2}{\iint_{4\pi}\left|F_i(\theta,\phi)\right|^2 d\Omega \cdot \iint_{4\pi}\left|F_j(\theta,\phi)\right|^2 d\Omega} \tag{1}$$

Here, $F_i(\theta,\phi)$ and $F_j(\theta,\phi)$ represent the far-field radiation vectors of the i-th and j-th antenna elements, respectively [25]. The ECC of the antenna is calculated across the entire frequency band for both the Sub-6 GHz and 5G mmWave bands, and the results are shown in Fig. 15.

As observed from Fig. 15, the ECC of the antenna remains below 0.003 across the entire operating frequency band (4.37–5.88 GHz, 23.53–32.89 GHz, and 36.8–40.1 GHz). This excellent low correlation is primarily attributed to two factors: first, the four radiating elements are arranged in an orthogonal and symmetric layout, forming inherent polarization and spatial diversity; second, the central cross-shaped isolation structure effectively suppresses electromagnetic coupling between ports, further reducing the signal correlation.

3.4. Diversity Gain

Diversity gain (DG) reflects the improvement in signal-to-noise ratio obtained by a MIMO system through multiple-antenna reception in a fading environment. For a two-port system, the relationship between DG and ECC can be expressed as Equation (2) [26]:

$$DG = 10\sqrt{1-|\rho|^2} \tag{2}$$

For a four-port MIMO system, the diversity gain between each pair of ports can be calculated, and the overall system diversity

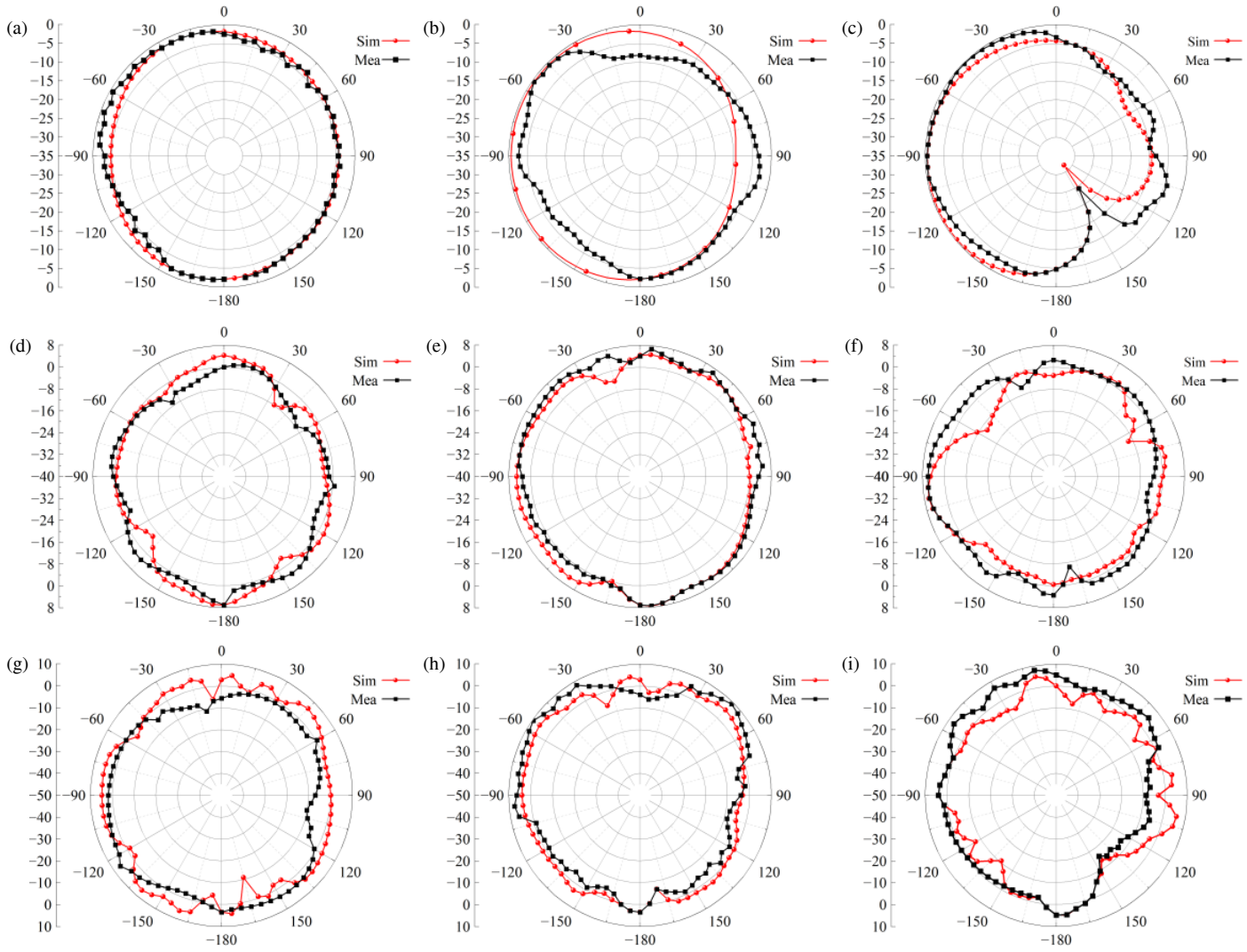

FIGURE 14. Radiation patterns. (a) yoz plane, (b) xoz plane, (c) xoy plane, (d) yoz plane, (e) xoz plane, (f) xoy plane, (g) yoz plane, (h) xoz plane, and (i) xoy plane.

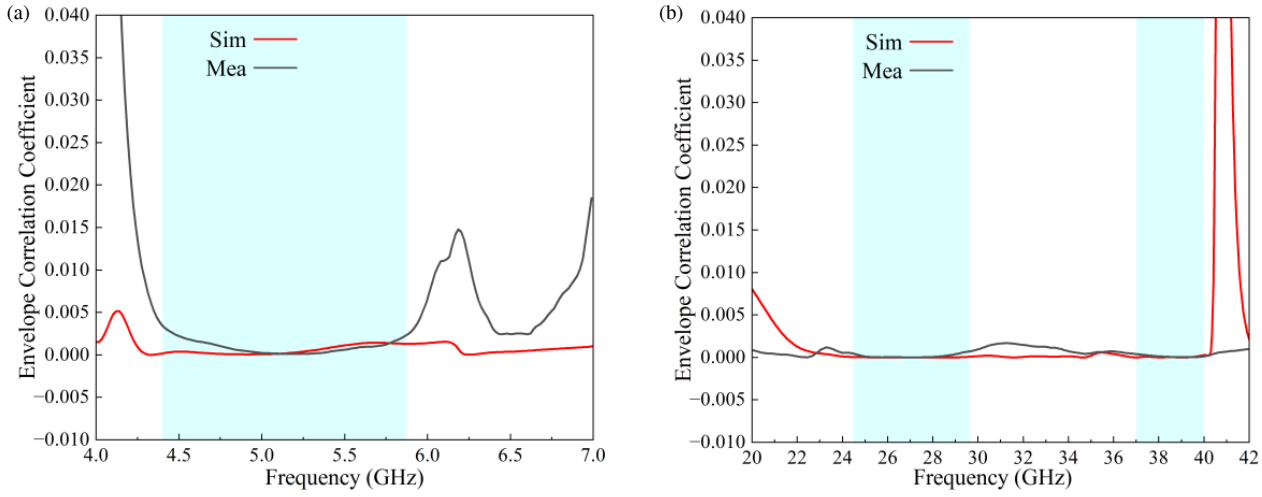

FIGURE 15. ECC between elements of the proposed antenna. (a) Sub-6 GHz ECC and (b) 5G mmWave ECC.

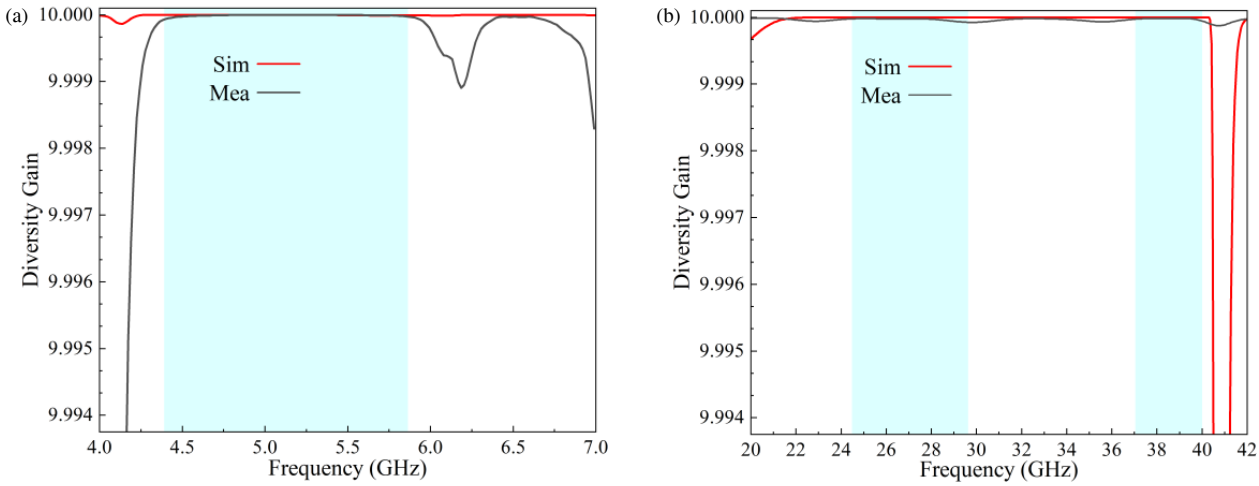

FIGURE 16. DG between elements of the proposed antenna. (a) Sub-6 GHz DG and (b) 5G mmWave DG.

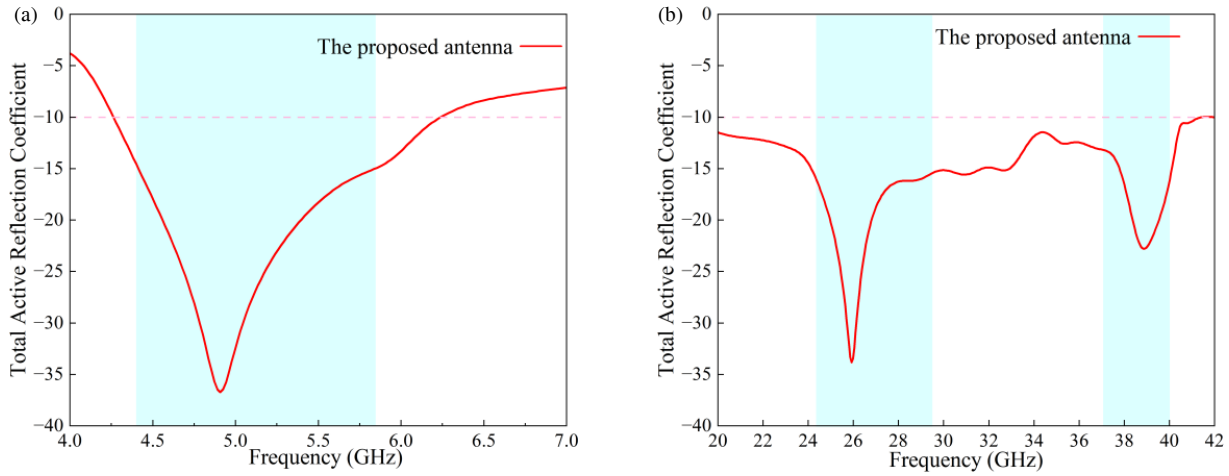

FIGURE 17. TARC between elements of the proposed antenna. (a) Sub-6 GHz TARC and (b) 5G mmWave TARC.

performance can be evaluated by taking the average or minimum value. The simulated and measured diversity gains for the Sub-6 GHz and 5G mmWave bands are shown in Fig. 16.

Based on the calculated ECC results, the diversity gain of the proposed antenna approaches the ideal value of 10 dB in the low-, mid-, and high-frequency bands, indicating that the MIMO antenna exhibits excellent diversity performance.

3.5. Total Active Reflection Coefficient

Total active reflection coefficient (TARC) reflects the impedance-matching characteristics of a MIMO antenna when multiple ports are simultaneously excited. It is defined as the square root of the ratio of the sum of reflected powers at all ports to the sum of the incident powers [27], as expressed in Equation (3):

$$\Gamma_a^t = \frac{\sqrt{\sum_{i=1}^{N} |b_i|^2}}{\sqrt{\sum_{i=1}^{N} |a_i|^2}} \tag{3}$$

For a four-port system, TARC can be calculated from S-parameters, as expressed in Equation (4):

$$\Gamma_a^t = \frac{\sqrt{\sum_{i=1}^{4} \left| \sum_{j=1}^{4} S_{ij} e^{j\theta_j} \right|^2}}{2} \tag{4}$$

Here, the denominator of 2 in Equation (4) originates from the equal-amplitude normalized excitation condition of the four-port MIMO antenna, and θ_2, θ_3, and θ_4 represent the excitation phases of the corresponding ports. Fig. 17 shows the total active reflection coefficient (TARC) obtained by averaging the results calculated from 12 randomly selected phase combinations of θ_2, θ_3, and θ_4.

As observed from Fig. 17, the TARC remains below -10 dB across the entire operating frequency band. In the low-frequency Sub-6 GHz band of 4.37–5.88 GHz, the TARC is below -10 dB and reaches a minimum of approximately -37 dB. In the 5G mmWave bands of 23.5–32.89 GHz and 36.8–40.1 GHz, the TARC is also below -10 dB, with a minimum of approximately -34 dB, which is generally consistent with the reflection characteristics of individual ports. This

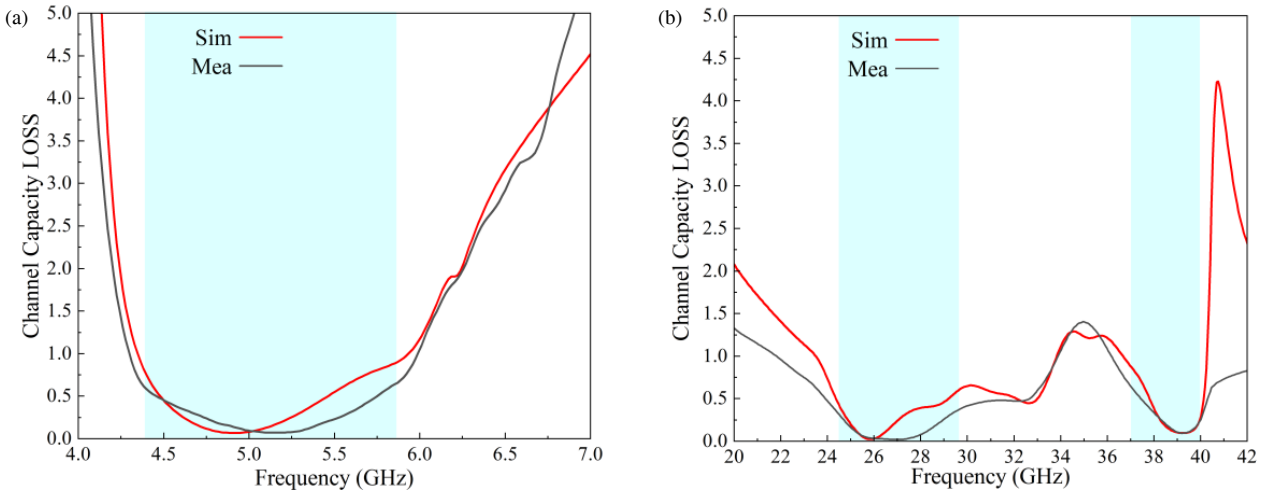

FIGURE 18. CCL between elements of the proposed antenna. (a) Sub 6 GHz CCL and (b) 5G mmWave CCL.

TABLE 2. Comparison between the reported and the proposed antennas.

References	Realize the frequency band (GHz)	Impedance bandwidth (GHz)	ECC	Peak gain (dBi)	Implementation complexity	Size (mm^3)
3	5G mmWave (27–30, 35.54–41)	3, 5.46	< 0.001	7.47.5	Easy	$38.6 \times 38.6 \times 0.787$
7	Sub 6 GHz (3.15–4.1)	0.95	< 0.04	3.6	Easy	$54.5 \times 54.5 \times 1.58$
8	Sub 6 GHz (4.4–5)	0.6	0.01	2.83	Easy	$45 \times 45 \times 1.2$
9	Sub 6 GHz (3.409–3.601, 4.76–5.04)	0.192, 0.28	< 0.05	——	Easy	$38.6 \times 54.6 \times 1.524$
11	Sub 6 GHz and 5G mmWave (4.4–5.6, 24.25–29.5)	1.6, 5.25	——	——	Complex	$70 \times 70 \times 0.508$
12	Sub 6 GHz and CMW (2.5–8.7, 9.2–16.7)	6.2, 7.5	< 0.03	3.5, 4.4, 6.67, 5.12	Easy	$32 \times 32 \times 1.6$
29	Sub-6 GHz and mmWave (5.29–6.12, 26–29.5)	0.83, 3.5	< 0.05, 0.005	5.13, 9.53	Easy	$75 \times 110 \times 0.76$
30	Sub-6 GHz and mmWave (2.18–7.15, 20.15–31.95)	4.97, 11.80	< 0.001, < 0.004	4.9, 11.5	Easy	$50 \times 50 \times 0.8$
This work	**Sub 6 GHz and mmWave (4.36–5.91, 23.81–33.72, 36.84–40.47)**	**1.55, 9.91, 3.63**	< 0.003 **< 0.001**	**0.95, 5.89 8.9**	**Easy**	$30 \times 30 \times 0.787$

indicates that, when multiple ports are simultaneously excited, the antenna maintains good impedance matching, and the mutual coupling between ports has a limited effect on the overall reflection performance.

3.6. Channel Capacity Loss

Channel capacity loss (CCL) reflects the reduction in capacity of a MIMO system under non-ideal channel conditions. A lower CCL indicates that the system can maintain higher data transmission rates [28]. For a four-port MIMO antenna, CCL can be calculated from the received signal correlation matrix, as expressed in Equation (5):

$$C_{loss} = -\log_2 \det\left(\psi^R\right) \tag{5}$$

Here, ψ_R is the receive correlation matrix, and its elements are calculated from the S-parameters:

$$\psi_{ij}^R = \begin{cases} 1 - \sum_{n=1}^{4} |S_{ni}|^2, & i = j \\ -\sum_{n=1}^{4} S_{ni}^* S_{nj}, & i \neq j \end{cases} \tag{6}$$

As shown in Fig. 18, the simulated and measured CCLs for the Sub-6 GHz and 5G mmWave bands are presented. The results indicate that, in the low-frequency band, the CCL is < 0.4 bits/s/Hz. In the mid-frequency band of the 5G mmWave, the maximum CCL does not exceed 1.0 bits/s/Hz, with most of the range below 0.6 bits/s/Hz. In the high-frequency band of the 5G mmWave. Overall, the antenna exhibits excellent channel

transmission capability in the Sub-6 GHz band, and the CCL characteristics in the 5G mmWave bands are sufficient to meet the high-data-rate communication requirements of 5G systems.

3.7. Antenna Performance Comparison

Table 2 provides a detailed comparison between the proposed antenna and those reported in other references. As shown in the table, Refs. [7–9] only cover the Sub-6 GHz band and do not provide coverage in the mmWave bands. Ref. [3] is mainly designed for mmWave applications but does not support Sub-6 GHz operation. Although multi-band coverage is achieved in [12], the 5G mmWave bands are not covered. Ref. [11] is capable of covering both the Sub-6 GHz and mmWave bands; however, its structure is relatively complex, which increases the fabrication difficulty. The antennas reported in [29] and [30] have relatively large dimensions and cannot cover the n260 band.

Compared with the antennas summarized in Table 2, the proposed antenna adopts an integrated and compact structure. Multi-band operation is achieved using a single radiating element, thereby avoiding the structural complexity and large size commonly associated with conventional multi-band antennas. In addition, stable electromagnetic performance is maintained, while simultaneous coverage of the Sub-6 GHz, Wi-Fi, and multiple 5G mmWave bands is achieved within a compact size. Furthermore, low ECC and high gain in the mmWave bands are obtained.

4. CONCLUSION

A miniaturized multi-band MIMO antenna for Sub-6 GHz and 5G mmWave applications is proposed in this work, with an overall size of only $30 \times 30 \times 0.787\,\text{mm}^3$. By employing a C-shaped radiating structure and multi-branch coupling techniques, the communication requirements of the n79, Wi-Fi 5/6, and 5 GHz ISM bands, as well as the 5G mmWave n257, n258, n261, and n260 bands, are satisfied. Measured results show that, under the condition of $S_{11} < -10\,\text{dB}$, tri-band coverage of 4.37–5.88 GHz, 23.5–32.89 GHz, and 36.8–40.1 GHz is achieved. In addition, the port isolation is better than $-20\,\text{dB}$, while the peak gains are 0.95 dBi, 5.89 dBi, and 8.83 dBi in the low-, mid-, and high-frequency bands, respectively. Furthermore, an ECC < 0.003 and a DG $> 9.93\,\text{dB}$ are obtained. Owing to its integrated structure, compact size, simple configuration, and excellent performance, the proposed antenna is capable of meeting the requirements of cooperative communication in the Sub-6 GHz and 5G mmWave bands.

ACKNOWLEDGEMENT

This work was supported by the Key Project of Natural Science Research of Colleges and Universities in Anhui Province under Grant 2023AH052650, 2025AHGXZK30493, by the Project of Scientific Research Starting for the High-level talents of West Anhui University under Grant WGKQ2022009, and by the Key Cultivation Project for Outstanding Young Teachers in Anhui Province China under Grant YQZD2024039.

REFERENCES

[1] Lin, X., "An overview of 5G advanced evolution in 3GPP release 18," *IEEE Communications Standards Magazine*, Vol. 6, No. 3, 77–83, 2022.

[2] Li, J., Y. Niu, H. Wu, B. Ai, S. Chen, Z. Feng, Z. Zhong, and N. Wang, "Mobility support for millimeter wave communications: Opportunities and challenges," *IEEE Communications Surveys & Tutorials*, Vol. 24, No. 3, 1816–1842, 2022.

[3] Sethi, W. T., S. H. Kiani, M. E. Munir, D. A. Sehrai, H. □. savci, and D. Awan, "Pattern diversity based four-element dual-band MIMO patch antenna for 5G mmWave communication networks," *Journal of Infrared, Millimeter, and Terahertz Waves*, Vol. 45, No. 5, 521–537, 2024.

[4] Awan, W. A., M. Soruri, M. Alibakhshikenari, and E. Limiti, "On-demand frequency switchable antenna array operating at 24.8 and 28 GHz for 5G high-gain sensors applications," *Progress In Electromagnetics Research M*, Vol. 108, 163–173, 2022.

[5] Jung, J., W. A. Awan, D. Choi, J. Lee, N. Hussain, and N. Kim, "Design of high-gain and low-mutual-coupling multiple-input–multiple-output antennas based on prs for 28 GHz applications," *Electronics*, Vol. 12, No. 20, 4286, 2023.

[6] Sharawi, M. S., "Printed multi-band MIMO antenna systems and their performance metrics [wireless corner]," *IEEE Antennas and Propagation Magazine*, Vol. 55, No. 5, 218–232, 2013.

[7] Dkiouak, A., A. Zakriti, M. Hefnawi, S. Chakkor, and K. E. Khadiri, "Compact high-isolation four-port MIMO antenna for 5G sub-6 GHz applications," *Progress In Electromagnetics Research C*, Vol. 160, 1–8, 2025.

[8] Kothavari, P. K. and V. R. Nuthakki, "A 5G NR n79 band compact MIMO antenna with DGS-based isolation enhancement," *Progress In Electromagnetics Research C*, Vol. 163, 187–197, 2026.

[9] Wang, W., Y. Wu, W. Wang, and Y. Yang, "Isolation enhancement in dual-band monopole antenna for 5G applications," *IEEE Transactions on Circuits and Systems II: Express Briefs*, Vol. 68, No. 6, 1867–1871, 2021.

[10] Islam, T., E. M. Ali, W. A. Awan, M. S. Alzaidi, T. A. H. Alghamdi, and M. Alathbah, "A parasitic patch loaded staircase shaped UWB MIMO antenna having notch band for WBAN applications," *Heliyon*, Vol. 10, No. 1, e23711, 2024.

[11] Saurabh, A. K. and M. K. Meshram, "Integration of sub-6 GHz and mm-Wave antenna for higher-order 5G-MIMO system," *IEEE Transactions on Circuits and Systems II: Express Briefs*, Vol. 69, No. 12, 4834–4838, 2022.

[12] Phaneendra, C. N. and K. K. Naik, "Inset-fed octagonal-shaped quad-port MIMO patch antenna for UWB applications," *Wireless Personal Communications*, Vol. 138, No. 2, 1311–1327, 2024.

[13] Çelik, K., "A novel band notched circular ring quad port UWB MIMO antenna," *Sādhanā*, Vol. 50, No. 3, 154, 2025.

[14] Yao, S., X. Qiu, and T. Yang, "A miniaturized UWB MIMO antenna design for 5G multi-band applications," *Progress In Electromagnetics Research C*, Vol. 153, 1–12, 2025.

[15] Liu, D., X. Gu, C. W. Baks, and A. Valdes-Garcia, "Antenna-in-package design considerations for Ka-band 5G communication applications," *IEEE Transactions on Antennas and Propagation*, Vol. 65, No. 12, 6372–6379, 2017.

[16] Liu, R., K. Ma, N. Yan, Y. Wang, and Y. Wu, "An FR4-based miniaturized high-efficiency double-sided SISL longitudinal slot antenna array for 5G millimeter-wave applications," *IEEE Transactions on Antennas and Propagation*, Vol. 72, No. 7, 6099–6104, 2024.

[17] Elabd, R. H., R. E. A. Shehata, A. J. A. Al-Gburi, and M. E. Mousa, "Compact and high-performance MIMO antenna with metasurface integration for millimeter-wave and next-generation 6G applications," *Journal of Infrared, Millimeter, and Terahertz Waves*, Vol. 46, No. 9, 62, 2025.

[18] Kim, S. and S. Nam, "Wideband and ultrathin 2 × 2 dipole array antenna for 5G mmWave applications," *IEEE Antennas and Wireless Propagation Letters*, Vol. 21, No. 12, 2517–2521, 2022.

[19] Jiang, Y., Z. Ke, K. Lu, and N. Yang, "A wideband Bowtie antenna fed with CPW for 5G mmWave applications," in *2024 15th Global Symposium on Millimeter-Waves & Terahertz (GSMM)*, 1–3, Hong Kong, 2024.

[20] Sim, C.-Y.-D., J.-J. Lo, and Z. N. Chen, "Design of a broadband millimeter-wave array antenna for 5G applications," *IEEE Antennas and Wireless Propagation Letters*, Vol. 22, No. 5, 1030–1034, 2023.

[21] Prasad, K. V., N. Venkateswari, M. Sandhyarani, P. V. Kumar, and K. M. Lakshmi, "Isolation and bandwidth enhancement of compact wideband MIMO for sub-6 GHz , ku-band and millimeter-wave with UWB applications," *Progress In Electromagnetics Research C*, Vol. 148, 83–95, 2024.

[22] Harrington, R. and J. Mautz, "Theory of characteristic modes for conducting bodies," *IEEE Transactions on Antennas and Propagation*, Vol. 19, No. 5, 622–628, 1971.

[23] Vaughan, R. G. and J. B. Andersen, "Antenna diversity in mobile communications," *IEEE Transactions on Vehicular Technology*, Vol. 36, No. 4, 149–172, 1987.

[24] Blanch, S., J. Romeu, and I. Corbella, "Exact representation of antenna system diversity performance from input parameter description," *Electronics Letters*, Vol. 39, No. 9, 705–707, 2003.

[25] Cheng, C., Y. Jia, and Y. Liu, "Channel-dependent envelope correlation coefficient parameters," in *2025 IEEE 8th International Symposium on Electromagnetic Compatibility (ISEMC)*, 1–3, Hefei, China, 2025.

[26] Manteghi, M. and Y. Rahmat-Samii, "Multiport characteristics of a wide-band cavity backed annular patch antenna for multipolarization operations," *IEEE Transactions on Antennas and Propagation*, Vol. 53, No. 1, 466–474, 2005.

[27] Chae, S. H., S.-k. Oh, and S.-O. Park, "Analysis of mutual coupling, correlations, and TARC in WiBro MIMO array antenna," *IEEE Antennas and Wireless Propagation Letters*, Vol. 6, 122–125, 2007.

[28] Kildal, P.-S. and K. Rosengren, "Correlation and capacity of MIMO systems and mutual coupling, radiation efficiency, and diversity gain of their antennas: Simulations and measurements in a reverberation chamber," *IEEE Communications Magazine*, Vol. 42, No. 12, 104–112, 2004.

[29] Iffat Naqvi, S., N. Hussain, A. Iqbal, M. Rahman, M. Forsat, S. S. Mirjavadi, and Y. Amin, "Integrated LTE and millimeter-wave 5G MIMO antenna system for 4G/5G wireless terminals," *Sensors*, Vol. 20, No. 14, 3926, 2020.

[30] Srinubabu, M., N. X. Sinh, T. Addepalli, X. Louangvilay, and N. V. Rajasekhar, "Design of integrated 4 × 4 MIMO antenna for sub 6-GHz and mm-wave operation using T-shaped isolation," *Physica Scripta*, Vol. 100, No. 5, 055541, 2025.